



Repositorio Institucional de la Universidad Autónoma de Madrid

<https://repositorio.uam.es>

Esta es la **versión de autor** del artículo publicado en:

This is an **author produced version** of a paper published in:

Chemistry - A European Journal 25.53 (2019): 12394-12404

DOI: <https://doi.org/10.1002/chem.201902052>

Copyright: © 2019 Wiley - VCH Verlag GmbH & Co. KGaA, Weinheim

El acceso a la versión del editor puede requerir la suscripción del recurso

Access to the published version may require subscription

Synergistic effect of covalent bonding and physical encapsulation of sulfur in the pores of a microporous COF to improve cycling performance in Li-S batteries

Sergio Royuela,^[a,b] Joaquín Almarza,^[a,c] María J. Mancheño,^[a] Juan C. Pérez-Flores,^[d] Enrique G. Michel,^[e,f] María M. Ramos,^[b] Félix Zamora,^[f,g,h,i] Pilar Ocón,^{*,[c]} José L. Segura^{*,[a]}

Abstract: Lithium-sulfur batteries stand out as a promising technology for energy storage owing to a combination of favorable characteristics including a high theoretical gravimetric capacity, energy density, inexpensive character and environmental benignity. Covalent organic frameworks (COFs) are a rapidly developing family of functional nanostructures which combine porosity and crystallinity and which have been already used in this kind of batteries to build sulfur electrodes by embedding sulfur into porous COFs in order to enhance cycle lifetimes. In this contribution, we go one step forward and we use a COF endowed with vinyl groups in order to graft sulfur to the COF skeleton through inverse vulcanization. The main aim of the article is to show the synergistic effect of covalent bonding and physical encapsulation of sulfur in the pores of the COF in order to alleviate the fatal redox shuttling process, to improve the cycling performance and to provide faster ion diffusion pathways. In addition, it is shown how the material with covalently bound S provides better

electrochemical performance under demanding and/or changeable charge conditions than a parent analogue material with sulfur physically confined but without covalent linkage.

Introduction

The use of Li-ion rechargeable batteries (LIB) has enabled the wireless revolution of portable electronics and offers good prospects for accelerating the development of battery electric automobiles.^[1] Lithium-Sulfur (Li-S) rechargeable batteries are a particular type of Li-ion batteries which are currently receiving a great deal of attention due, among others, to the competitive values of theoretical gravimetric capacity (above 1600 mA h g⁻¹) and energy density (above 2500 W h kg⁻¹).^[2] Additional features that make this family of batteries especially attractive are their relatively inexpensive character and their environmental benignity taking into account the natural abundance and nontoxicity of sulfur. In this respect, it is worth pointing out that a large amount of the world's sulfur is obtained from gas and petroleum sources as a secondary product in the hydrodesulphurization process in the petroleum refining industry.^[3] However, there are still some challenges that Li-S batteries have to face before they become a realistic and cheap energy supply. Thus, the internal diffusion of soluble polysulfide intermediates in the organic electrolytes during the processes of charge and discharge has been identified as the main cause of the so-called redox shuttling process which is responsible for the still limited cycle lifetimes in Li-S batteries.^[4]

In this regard, the physical confinement of elemental sulfur within porous media has been proposed as a strategy to minimize the redox shuttling process.^[5] With this aim, macromolecular microporous systems with precisely defined pore sizes can be used in order to simultaneously facilitate the aprotic electrolyte permeation as well as the diffusion of ions. In fact, it has been already shown in Li-ion rechargeable batteries that structuring microporous polymer framework electrodes with both easy electron transfer and Li⁺ diffusion is of great significance.^[6] However, the total confinement of sulfur within these porous architectures is technically unattainable and therefore a certain dissolution of the soluble polysulfide intermediates during the battery cycling cannot be ruled out.^[7]

Binding sulfur and carbon through strong covalent bonds has been recently identified as an efficient strategy in order to avoid this problem with the soluble polysulfide intermediates.^[8] With this aim, Pyun and co-workers^[8b, 8c] have developed the "inverse vulcanization" strategy to prepare sulfur-rich copolymers as active cathode materials for Li-S batteries. The strategy involves the bulk radical copolymerization of suitably functionalized monomers in the presence of molten sulfur at a

-
- [a] S. Royuela, Dr. M. J. Mancheño, Dr. J. L. Segura
Departamento de Química Orgánica I, Facultad de CC. Químicas
Universidad Complutense de Madrid
Madrid 28040, Spain
E-mail: segura@quim.ucm.es
- [b] S. Royuela, Dr. M. M. Ramos
Departamento de Tecnología Química y Ambiental
Universidad Rey Juan Carlos
Madrid 28933, Spain
- [c] J. Almarza, Dr. P. Ocón
Departamento de Química Física Aplicada, Facultad de Ciencias
Universidad Autónoma de Madrid
Madrid 28049, Spain
Email: pilar.ocon@uam.es
- [d] Dr. J. C. Pérez-Flores
Instituto de Energías Renovables
Universidad de Castilla-La Mancha
Albacete 02006, Spain
- [e] Dr. E. G. Michel
Departamento de Física de la Materia Condensada
Universidad Autónoma de Madrid
Madrid 28049, Spain
- [f] Dr. E. G. Michel, Dr. F. Zamora
Condensed Matter Physics Center (IFIMAC)
Universidad Autónoma de Madrid
Madrid 28049, Spain
- [g] Dr. F. Zamora
Departamento de Química Inorgánica, Facultad de Ciencias
Universidad Autónoma de Madrid
Madrid 28049, Spain
- [h] Dr. F. Zamora
Institute for Advanced Research in Chemical Sciences (IAdChem)
Universidad Autónoma de Madrid
Madrid 28049, Spain
- [i] Dr. F. Zamora
Instituto Madrileño de Estudios Avanzados en Nanociencia (IMDEA-Nanociencia)
Madrid 28049, Spain

Supporting information for this article is given via a link at the end of the document.

temperature above that in which the radical ring-opening polymerization of S_8 takes place. Furthermore, Park et al.^[9] and Choi et al.^[10] prepared three-dimensionally interconnected polymers with high sulfur content based on triazine moieties linked through sulfur chains. These novel macromolecular systems in which the polysulfide intermediates are confined and covalently attached to the porous polymer networks have been used for the fabrication of Li-S batteries with high specific capacities and excellent capacity retention during cycling.^[9] This work shows the benefits of covalent binding sulfur and carbon through strong covalent bonds in this kind of porous systems in order to improve cycling performance.

Therefore, it is clear the need to develop organic frameworks with ordered pore structures that enable regular sulfur distribution, with large voids for sulfur loading, and that allow robust sulfur binding in order to achieve efficient and reliable Li-S batteries. In this context, covalent organic frameworks (COFs) exhibit structures that can be controlled with atomic precision by connecting multidentated organic building blocks through dynamic covalent-bond formation. Among them, COFs linked in two dimensions (2D-COFs) are of great interest because π -stacking between the 2D-COF layers allows a predictable and deliberate organization of the functional organic building blocks into insoluble, high-surface porous polymer networks. When the 2D-COF layers are arranged with an eclipsed stacking, 1D defined nanoscale porous channels are generated that run alongside the stacking direction.^[11]

Due to the unique characteristics of COFs, in the last recent years scientist from many different areas including synthetic chemists and materials scientists have jumped into the field developing a variety of materials with applications in areas such as catalysis, storage and separation of gases, separation from solutions, optoelectronics, drug delivery or sensing among others.^[12] In this respect, it is worth mentioning that 2D-COFs have also found applications in the field of electrochemical energy storage^[13] where 2D-COFs have been used not only as active materials^[14] but also as hosts for active materials^[10, 15] in rechargeable Li-ion batteries.

Recent research of Ai, Wang and coworkers showed that the distinctive oriented porous channels of 2D-COFs are suited to be impregnated with sulfur (i) because the aggregation of sulfur is restricted and (ii) specially because the diffusive loss of soluble polysulfide intermediates can be efficiently suppressed.^[16] Furthermore, the post-synthetic modification (PSM) of 2D-COFs with sulfur has been also addressed in order to produce materials that have been efficiently used as cathodes in Li-S batteries.^[17] Thus, PSM has revealed as an efficient strategy in order to complement the unique characteristics of the ordered porous structure of COFs and broaden the scope of their functionalities.^[18]

In this article: (i) we reproduce the synthesis of a porphyrin-based 2D-COF (**H₂P-COF**, Figure 1)^[15a] with a regular pore structure and large void spaces as host material for sulfur storage; (ii) we describe the synthesis of a new analogous 2D-COF (**H₂P-COF-BATA**, Figure 1) endowed with accessible allyl moieties in the nanochannels. This novel COF allows for sulfur

loading by diffusion upon heating at 120 °C followed by robust C-S binding through the inverse vulcanization process with thermal activation at 185 °C. The inverse vulcanization process involves the bulk radical copolymerization between sulfur and the allyl groups in the COF's channels at a temperature above that in which the radical ring-opening polymerization of S_8 takes place.

The electrochemical performances of the COF used as host material for sulfur as well as the inverse-vulcanized COF have been investigated in coin-type half-cells. The main aim of the article is to study the combined effect of covalent bonding and physical encapsulation of sulfur in the pores of COFs in order to improve the cycling performance, to provide faster ion diffusion pathways and to alleviate the redox shuttling process in Li-S batteries.

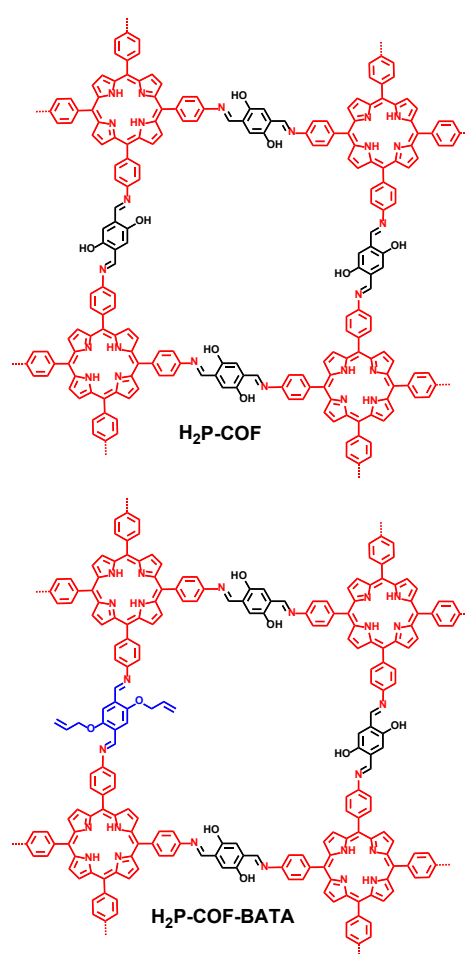
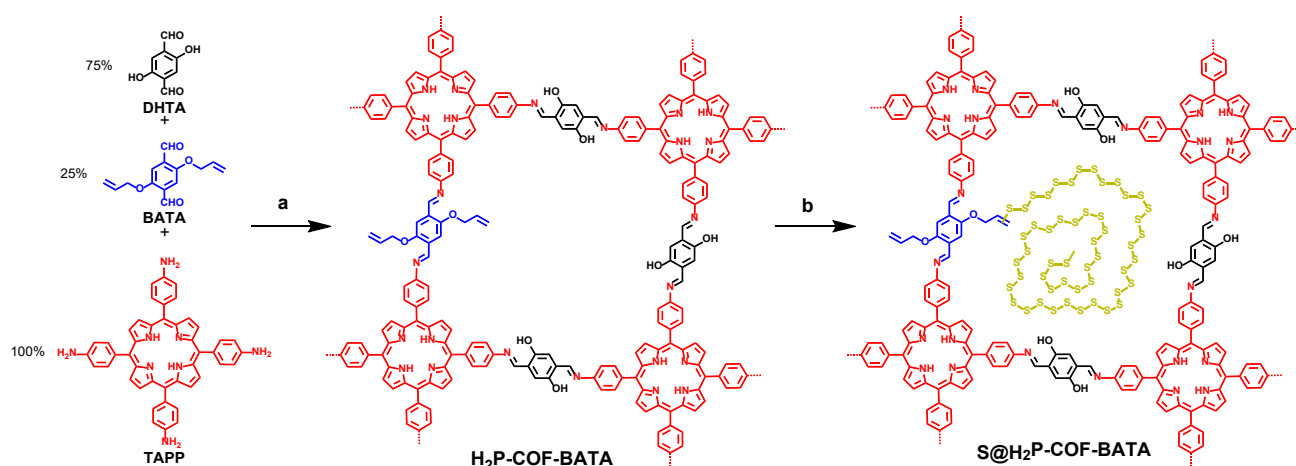


Figure 1. Chemical structure of **H₂P-COF** and **H₂P-COF-BATA**.



Scheme 1. Synthesis of **H₂P-COF-BATA** and **S@H₂P-COF-BATA**. a: oDCB/nBuOH/AcOH 3 M 1:2:0.3, 120 °C, 6 d. b: Elemental sulfur, (i)120 °C/overnight, (ii) 185 °C/8 h, (iii) 185 °C/2 h.

Results and Discussion

For the design of the sulfur host materials several aspects were considered. Firstly, we have used porphyrin-based COFs because of the characteristic efficient π - π stacking of the porphyrin moiety which provide robust COF skeletons with eclipsed stacking alignments and suitable nanochannels for sulfur loading.^[19] Therefore we chose 5,10,15,20-tetrakis(4-aminophenyl)-21*H*,23*H*-porphyrin (**TAPP**) as the tetragonal unit. Secondly, hydroxyl functionalities in 2,5-dihydroxyterephthalaldehyde (**DHTA**) have shown the ability to form O-H...C=N interactions with the imine nitrogen leading to a planarization of the COF structure and a higher crystallinity.^[20] Additionally, this monomer can be easily modified to 2,5-bis(allyloxy)terephthalaldehyde (**BATA**) in order to endow the cavities of the COF with reactive allyl moieties, which can be used to trap sulfur in the COF pores. Therefore, we choose a 3:1 mol ratio of **DHTA/BATA** to obtain a new COF, hereafter named **H₂P-COF-BATA**, with high stability and reactive groups suitable for sulfur immobilization (Scheme 1). This **DHTA/BATA** ratio is enough to graft sulfur to the COF. Furthermore, adding more allyl substituents in the pore would compromise the porosity of the networks and therefore would produce inefficient sulfur incorporation. A COF formed only by **TAPP** and **DHTA**, without the allyl moieties (**H₂P-COF**), was also synthesized to study the effect of the covalent grafting of polysulfides to the COF.

The formation of the imine-based **H₂P-COF-BATA** was confirmed by ¹³C CP-MAS solid-state NMR spectrum, Fourier transform infrared spectroscopy (FTIR), powder X-ray diffraction (PXRD), nitrogen adsorption isotherm measurements (Figure 2) and X-ray photoelectron spectroscopy (XPS) (Figures 3, S2-S7). The ¹³C Cross Polarization Magic Angle Spinning (CP-MAS) solid-state NMR spectrum of **H₂P-COF-BATA** (Figure S8) shows

a group of signals corresponding to the sp^2 carbon atoms of the material and confirms the formation of the imine bond by the characteristic signal at δ 163 ppm, which corresponds to the chemical shift of the -C=N carbon. The FTIR spectrum shows the disappearance of the characteristic bands of the starting materials, *i.e.* the carbonyl bands at 1668 and 1679 cm^{-1} from the aldehydes and the NH₂ stretching band at 3300-3400 cm^{-1} from the amines; in addition, it can be observed the emergence of the characteristic stretching vibration of the C=N bond at 1614 cm^{-1} . After sulfur incorporation, the main absorption bands of **H₂P-COF-BATA** remain unchanged and a new band is observed at 670 cm^{-1} assigned to the vibration of the C-S bond (Figure 2b).^[17a, 21] Similar results were observed for **H₂P-COF**, the characteristic ¹³C NMR C=N signal at δ 163 ppm, the disappearance of the carbonyl and amine FTIR bands and appearance of the C=N vibration, but, as expected, no C-S bond was observed after sulfur impregnation (Figures S1a, S9).

The chemical bonding nature in **H₂P-COF** and **H₂P-COF-BATA** upon sulfur treatment has been also investigated by XPS of C_{1s}, N_{1s} and S_{2p}. In addition, synchrotron-based XPS spectra of S_{2p} have been investigated. The XPS N_{1s} spectra of **S@H₂P-COF** and **S@H₂P-COF-BATA** (Figures S2, S3) reveal the existence of two components, a main one with a binding energy (BE) of 400.0 eV and a minor one with a BE of 398.4 eV. In agreement with previous findings,^[22] the two components can be attributed to the three types of nitrogens found in **S@H₂P-COF** and **S@H₂P-COF-BATA**, the main one to the pyrrole-type and the imine-type, whose N_{1s} BEs are 400 eV and 399.3 eV respectively, and the minor one to the aza-type, whose N_{1s} BE is near 398 eV. The intensity ratio of 2.5 (3+2/2) is in agreement with this interpretation. The XPS C_{1s} spectra of **S@H₂P-COF** and **S@H₂P-COF-BATA** (Figures S4, S5) reveal a peak that can be deconvoluted in three components with binding energies of 285.0, 286.5, and 288.9 eV. The binding energy of 285.0 eV can be associated to -C=C-, while those of 286.5, and 288.9 eV can be attributed to the different components of the C-N bonds: the

former to the imine and pyrrole N and the latter to the aza N. The relative intensities of the three C_{1s} components are in agreement with the expected abundance of each type of C bond in **S@H₂P-COF** and **S@H₂P-COF-BATA**.^[10] An additional component in the C_{1s} core level at a higher BE of 292.1 eV is due to the organic polymer used to prepare the pellet suitable for analysis in UHV. The minor amounts of vinyl linkages in the COF accounts for the negligible contribution of a signal corresponding to the C-S bonding, which cannot be appreciated in the spectrum.

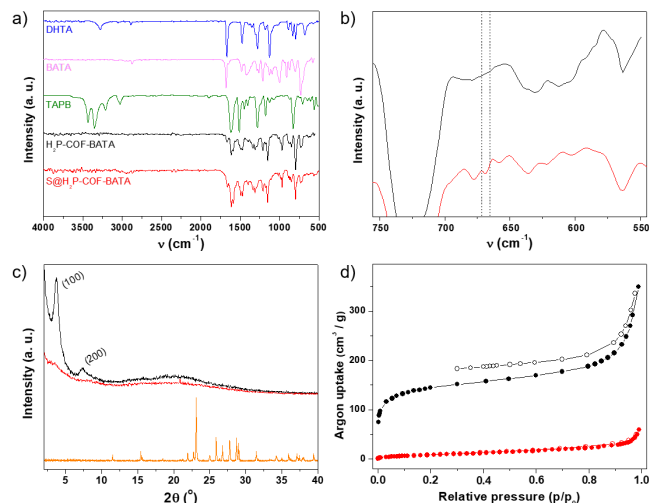


Figure 2. a) FTIR of **DHTA**, **BATA** and **TAPP** monomers, **H₂P-COF-BATA** and **S@H₂P-COF-BATA**. b) Detailed comparison of the FTIR spectra of **H₂P-COF-BATA** (black) and **S@H₂P-COF-BATA** (red) showing the C-S stretching vibration at 670 cm^{-1} . c) XRD of **H₂P-COF-BATA** (black), **S@H₂P-COF-BATA** (red) and elemental sulfur (orange). d) Argon adsorption isotherms of **H₂P-COF-BATA** (black) and **S@H₂P-COF-BATA** (red).

On the other hand, the two components of the S_{2p} doublet (3/2 and 1/2) are separated approximately by 1.2 eV. The XPS S_{2p} spectra for both **S@H₂P-COF** and **S@H₂P-COF-BATA** (Figures S6, S7) show at least two of these doublets, one with energy around 164.3 eV and a second one around 168.9 eV. The doublet at 164.3 eV can be assigned to the formation of S-S bonds in sulfur chains formed after thermal treatment.^[8c, 17a] The additional doublet around 168.9 eV can be attributed to the characteristic sulfate species formed by oxidation of sulfur in air.^[23] Again, the minor amounts of vinyl linkages in the material accounts for the negligible contribution of a signal corresponding to the C-S bonding which cannot be appreciated in the spectrum.

In order to detect the contribution corresponding to the linkage of sulfur to the COF networks we have investigated the synchrotron-based XPS spectrum of S_{2p} for **S@H₂P-COF-BATA**. The spectrum obtained (Figure 3) can be deconvoluted into three peaks. Besides the sulfate species near 168.2 eV, two additional doublets are observed. The main doublet at 164.3 eV can be attributed to the $S_{2p_{1/2}}$ and $S_{2p_{3/2}}$ of C-S_n-C chain ($n = 5, 6$) bonds in sulfur.^[23b, 24] An additional doublet is observed at a lower BE of 162.2 eV. This component and its lower BE confirm

the successful anchoring of the linear polysulfides with radical chain ends, which attack the vinyl units to form the C-S bonds.^[8c] The fraction of sulfur atoms bonded to C atoms is approximately a 30 % of the total S atoms detected under these conditions. The fraction of S atoms bonded to C can be used to estimate the number of C atoms bonded to them. Taking into account the different photon energies used, the cross sections of C_{1s} and S_{2p} at these energies, and the electron-analyzer transmission function, the calculation shows that C atoms bonded to S are approximately a 1 % of all carbon atoms with C=C bonds.

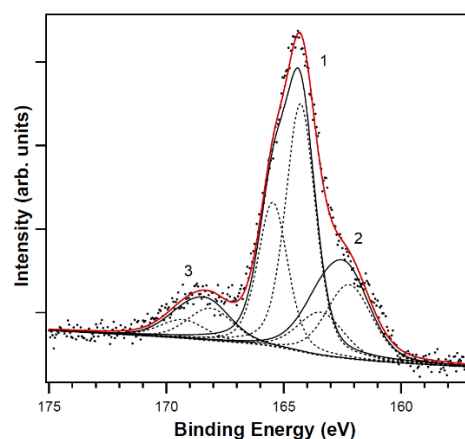


Figure 3. S 2p peak for the **S@H₂P-COF-BATA** sample ($h\nu = 850$ eV). Numbers identify the different components (black lines): **1** (S-S bonds in sulfur chains), **2** (C-S bonds) and **3** (sulfate). Each component corresponds to an S 2p doublet (dashed lines). Black dots are experimental points and the red line is the results of fit.

PXRD of both **H₂P-COF-BATA** and **H₂P-COF** showed an identical profile with an intense peak at 3.8 ° as well as a smaller one at 7.4 ° (Figure 2c, S1b). These correspond to the (100) and (200) reflections of a tetragonal (P4/m) unit cell with cell parameters $a = b = 25.6$ Å, $c = 4.0$ Å and $\alpha = \beta = \gamma = 90$ °, as reported in previous works.^[19b, 20, 25] As expected, the introduction of the small allyl moiety did not bring about any significant change in the diffractogram, indicating that the framework's structure remains unaltered. Similar results have been previously observed with the introduction of different functionalities in COFs' pores,^[26] including propargyl^[25, 27] or azidomethyl^[28] moieties. After sulfur grafting, PXRD of **S@H₂P-COF-BATA** and **S@H₂P-COF** showed a featureless pattern, indicating that sulfur was highly dispersed inside the COF pores. The disappearance of the diffraction signals in COF/S composites has been observed for other COFs composed of light-weight elements in which the sulfur is highly dispersed in the COF matrix.^[29] It deserves to be noted that the **H₂P-COF** diffraction peaks are recovered after removal of sulfur from the composite, indicating that the crystal structure of the COFs is stable after sulfur infiltration.

The porosity of the materials was studied by argon adsorption isotherms at 87 K. **H₂P-COF-BATA** and **H₂P-COF** showed a type I isotherm with a significant uptake in the low-pressure

region (Figures 2d, S1c), which is characteristic of microporous materials. In fact, pore size distributions determined by nonlocal density functional theory (NLDFT) of both materials showed profiles centered at 1.42 nm for **H₂P-COF-BATA** and 1.51 nm for **H₂P-COF** (Figure S12). The Brunauer-Emmett-Teller (BET) surface area and pore volume for **H₂P-COF-BATA** were calculated to be 435 m² g⁻¹ and 0.187 cm³ g⁻¹, respectively, and decreased to 34 m² g⁻¹ and 0.014 cm³ g⁻¹ after sulfur incorporation. On the other hand, impregnation of sulfur into **H₂P-COF** decreased its BET surface area from 490 to 38 m² g⁻¹ and its pore volume from 0.187 to 0.014 cm³ g⁻¹.

Thermogravimetric analysis (TGA) showed that **H₂P-COF-BATA** and **H₂P-COF** are stable up to 400 °C. The thermogram of the impregnated samples showed a new loss starting at 190 °C, corresponding to sulfur elimination (Figure S13). From these data the sulfur incorporations were calculated to be 10 % for **H₂P-COF-BATA** and 8 % for **H₂P-COF**.

Finally, all the materials were examined by scanning electron microscopy (SEM) revealing a flake-like morphology. This texture was maintained after sulfur impregnation and no bulk sulfur was observed (Figure S14). Elemental maps obtained by energy-dispersive X-ray (EDX) analysis exhibited a homogeneous distribution of C, N and O in **H₂P-COF-BATA** and **H₂P-COF**, which can be attributed to the skeleton of the frameworks. The mappings of **S@H₂P-COF-BATA** and **S@H₂P-COF** showed the presence of sulfur with a similar distribution to that of C, N and O, (Figures S15, S16) confirming its successful incorporation into the pores of the COFs.

Figure 4a shows the cyclic voltammetry (CV) comparison profiles of cells with **S@H₂P-COF** and **S@H₂P-COF-BATA** cathodes vs. lithium anode at 0.1 mV s⁻¹ as well as in the increasing range from 0.1 to 1.0 mV s⁻¹ in the 2.70 to 1.80 V voltage range. For **S@H₂P-COF**, two cathodic peaks appear (A and B in Figure 4a) located at 2.35 and 2.10 V in agreement with the conversion of S₈ towards long-chain lithium polysulfides Li₂S_n (n = 8, 4) and their further reduction to Li₂S₂/Li₂S, respectively.^[17a, 30] An anodic process follows with the development of two peaks (C and D in Figure 4a) at 2.31 and 2.43 V corresponding with the reversible oxidation from Li₂S₂/Li₂S to S₈. Similar processes can be found for **S@H₂P-COF-BATA**, although its peak positions, 2.30 and 2.00 V in discharge and 2.37 and 2.45 V in charge, respectively, show redox processes with lower reversibility in comparison to that of **S@H₂P-COF**.^[14]

These results are also consistent with the discharge/charge curves depicted in Figure 5. When the CV scan rate was increased, peaks B and C gradually overlap (Figure 4b and c), owing to a severe polarization during the lithiation/delithiation process.

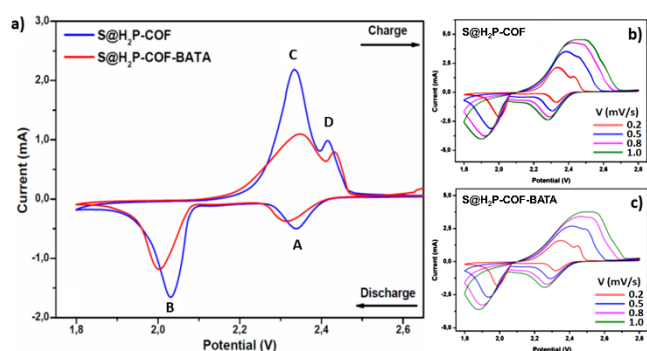


Figure 4. (a) Cyclic voltammetry for **S@H₂P-COF** (blue) and **S@H₂P-COF-BATA** (red) vs. Li⁺/Li at 0.1 mV s⁻¹. (b) Cyclic voltammetry for **S@H₂P-COF** at increasing rate from 0.2 V to 1 mV s⁻¹ in the 2.7 to 1.8 V voltage range. (c) Cyclic voltammetry for **S@H₂P-COF-BATA** at increasing rate from 0.2 V to 1 mV s⁻¹ in the 2.7 to 1.8 V voltage range.

Figure 5a shows the discharge-charge curves of the **S@H₂P-COF** cathode at a current rate of 0.1C in the voltage range of 1.8-2.7 V. Specific capacity and current rate referred to capacity values are obtained based on the sulphur mass and the theoretical specific capacity of a lithium-sulphur battery, 1675 mA h g⁻¹. During the first reduction, the **S@H₂P-COF** cathode shows a two-staged potential profile with a short pseudo-plateau at 2.35 V and a longer one at a lower potential, 2.10 V, which is assigned to the reduction from sulphur to high-order lithium polysulfides (Li₂S_n, 4 < n < 8) and the further reduction to solid lithium polysulfide Li₂S₂ and Li₂S, respectively. Following the charge process, two charge pseudo-plateaus are found at potentials of ≈ 2.25 V and ≈ 2.37 V, characterizing the inverse conversion of Li₂S₂ and Li₂S to Li₂S_n (4 < n < 8) and finally to S₈. Figure 5b shows the corresponding coulombic efficiency and discharge capacity for this lithium-sulfur cell in the same conditions described above. These results show an increasing efficiency up to a modest value close to 90 % of the theoretical one and exhibit a trend to stabilize a discharge specific capacity around 900 mA h g⁻¹ after 100 cycles, with a significant dispersion of values. This behavior could be attributed to the shuttle effect, especially noteworthy at low charge current densities, as in the current example.^[31]

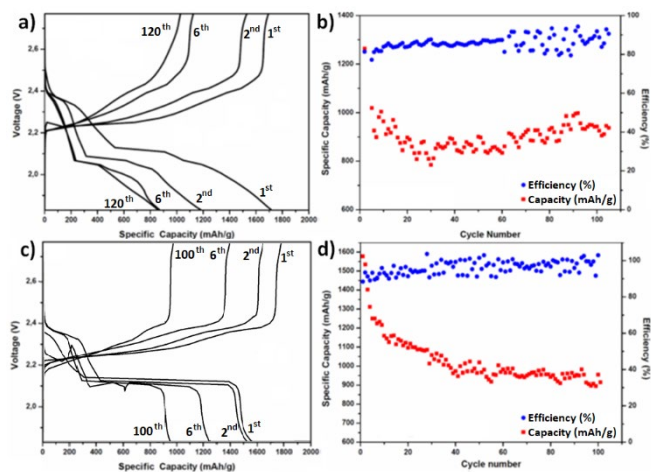


Figure 5. Galvanostatic discharge/charge electrochemical profile of **S@H₂P-COF** (a) and **S@H₂P-COF-BATA** (c). Cycle stability and Coulombic efficiency of **S@H₂P-COF** (b) and **S@H₂P-COF-BATA** (d) at 0.1C in the 2.7 to 1.8 V voltage range vs. Li⁺/Li.

The same electrochemical characterization is depicted in Figure 5c and 5d for **S@H₂P-COF-BATA** showing similar features to those found for **S@H₂P-COF**. The electrochemical discharge/charge processes show two main peaks at 2.30 and 2.05 V for reduction and 2.30 and 2.39 V for oxidation, corresponding to the S₈ conversion steps towards Li₂S₂/Li₂S and their corresponding reversible ones. This cell yields around 1600 mA h g⁻¹ during the first discharge cycle, close to the theoretical performance of the **S@H₂P-COF** battery, 1675 mA h g⁻¹. On the other hand, Figure 5d exhibits the cycling performance of the **S@H₂P-COF-BATA** cathode, with a discharge capacity around 900 mA h g⁻¹ and a coulombic efficiency close to 95 % after 100 cycles. In this case, although cycling values are close to those found for **S@H₂P-COF**, a remarkable improvement during extended cycling regarding the electrochemical stability is observed, indicating a significantly depressed shuttle effect of the polysulfide intermediates.

The cell performance assessment is broadened by the stepwise increase of the current rate every ten cycles (Figure 6). In the first cycle, at 0.1C, 0.2C and 0.5C, **S@H₂P-COF** and **S@H₂P-COF-BATA** batteries deliver a specific capacity of 975, 520 and 150 mA h g⁻¹ and 1200, 550 and 190 mA h g⁻¹ of their corresponding rates, respectively (Figure 6a and 6c). It is worth mentioning that when the charge/discharge rate returns to the initial 0.1C rate, **S@H₂P-COF** and **S@H₂P-COF-BATA** cells exhibit 810 and 1100 mA h g⁻¹ specific capacities, respectively. Therefore, the organic framework of **S@H₂P-COF-BATA** provides not only higher capacity and cycle ability performance in its corresponding Li-S battery, but also improves the rate capability.

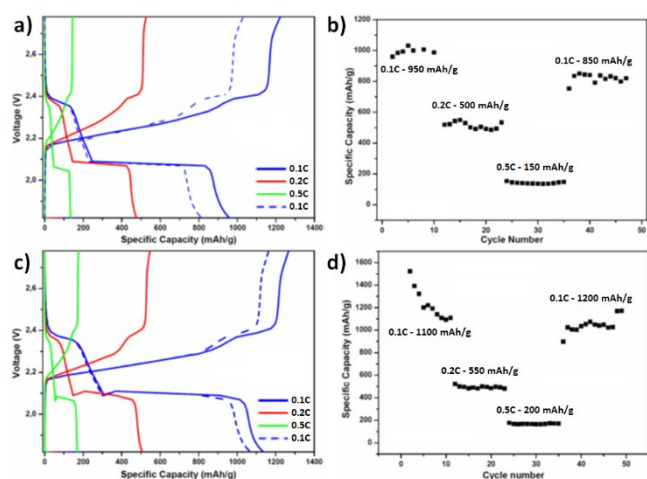


Figure 6. Galvanostatic discharge/charge electrochemical profile of **S@H₂P-COF** (a) and **S@H₂P-COF-BATA** (c) at different scan rates. Discharge capacity at different scan rates, 0.1C, 0.2C, 0.5C, 1.0C and 0.1C, of **S@H₂P-COF** (b) and **S@H₂P-COF-BATA** (d) in the 2.7 to 1.8 V voltage range vs. Li⁺/Li.

These results suggest that the covalent linkage of the sulfur intermediates into the nanopores of **S@H₂P-COF-BATA** inhibits sulfur release due to solubilization more effectively and, consequently, improves both the shuttle effect and the cycling performance of the battery.

Additionally, electrochemical impedance spectroscopy (EIS) characterization was carried out in order to gain knowledge about the electrochemical features of both **S@H₂P-COF** and **S@H₂P-COF-BATA** materials under progressive degradation due to working conditions. Thus, EIS measurements were developed upon cells with starting material before cycling, after 100 cycles at 0.1C and after cycling at different scan rates (Figure 7).

In general, the impedance spectra (Nyquist plot) show a depressed semicircle in the high-medium frequency and an oblique line in the low frequency region. The intercept on the real axis at high frequency represents the ohmic resistance including the electrolyte and all internal/external half-cell contacts. The semicircle at high-medium frequency is related with the transfer through the solid-electrolyte interface (SEI) and charge transfer resistance of the electrolyte/active material interface and the sloping line at low frequency is related to the Li-ion diffusion in the solid material.

Experimental data were analysed using $R_s(CPE_1[R_{CT}W])$ as the equivalent circuit that describes the processes involved in the study (see inset in Figure 7), according to the Boukamp's notation.^[32]

The equivalent circuit considers R_s as the electrolyte ohmic resistance; R_{CT} in parallel to CPE_1 , both refer to the corresponding ionic resistance and constant phase element due to the solid-electrolyte interface, SEI, and the charge-transfer resistance of the active material. It appears as a high-medium frequency arc (10⁶-20 Hz). In all cases, the capacity of the material has been simulated with a constant phase element given the characteristics of nanostructured electrodes, *i.e.* their

porous structure and the high roughness of the interface. Finally, below 20 Hz a $\approx 45^\circ$ leaning line is identified as a Warburg impedance element, Z_W , corresponding to a semi-infinite diffusion region and related to the Li ionic diffusion into the material.

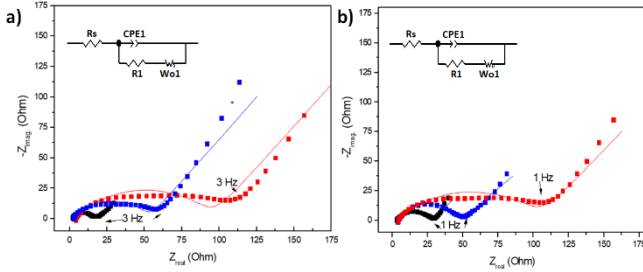


Figure 7. Nyquist plot of **S@H₂P-COF** (a) and **S@H₂P-COF-BATA** (b) at different conditions: initial (black lines), after 100 cycles at 0.1C (red lines) and after 100 cycles at different scan rates (blue lines).

The EIS spectra regarding the non-cycled cells show no significant differences, suggesting that the covalent binding of sulphur within the organic framework does not play a fundamental role at this stage. For R_s and CPE_1 , the values are 2.3 and 3.3Ω for **S@H₂P-COF**, and $5.8 \cdot 10^{-5}$ and $4.3 \cdot 10^{-5} F cm^{-1}$ for and **S@H₂P-COF-BATA**, respectively.

However, the resistance values obtained in R_{CT} , 15.7 and 24.1Ω for **S@H₂P-COF** and **S@H₂P-COF-BATA**, respectively, are significantly different. Indeed, the process in **S@H₂P-COF-BATA** initially appears to be kinetically disfavoured compared to that of **S@H₂P-COF**. At lower frequencies, 0.1-0.01 Hz, a straight line with 45° slope appears on the Nyquist plot, which is related with the semi-infinite dimension of the diffusion layer in the pore. This capacitive behaviour can be due to the accumulation of Li ions inside the solid.

After the continuous cycling at 0.1 C, 100 cycles, there is an increase in R_s which is attributed to the viscosity increase as a result of the presence of lithium polysulfides in the electrolyte. Furthermore, the electrochemical processes involved in the medium frequency element, R_{CT} increases up to 97.5 and 69.7Ω for **S@H₂P-COF** and **S@H₂P-COF-BATA**, respectively, being more significant the change observed for **S@H₂P-COF**. Therefore, the kinetic of the charge/discharge reaction improves considerably upon cycling for **S@H₂P-COF-BATA**, which has to be attributed to an increase of specific area and/or shortening of the ion transport pathways. Additionally, the CPE_1 value in **S@H₂P-COF** changes up to one order of magnitude towards a more capacitive process, leading to higher difficulty in the related charge transfer process, due to a better development of the electrochemical double layer resulting from the adsorption process in the electrode-electrolyte interface. In general, the variation of these elements could probably be related with the dispersion of specific capacity values in the **S@H₂P-COF** battery as previously commented.

On the other hand, after variable scan rate test, the R_{CT} increases for both electrodes while it remains lower than that

observed for continuous cycling at 0.1C; values of 50.9 and 43.5Ω for **S@H₂P-COF** and **S@H₂P-COF-BATA** are obtained, respectively (EIS fitting data in Supporting Table 2). The same considerations as those highlighted above in terms of improvement of the charge transfer process kinetics are assumed, but now an additional hint regarding a higher improvement as consequence of the variable charge/discharge current must be included. Again, **S@H₂P-COF** increases its capacitive behaviour according to the CPE_1 value.

The estimation of Li^+ diffusion coefficients (D_{Li}) for both cathodes can be developed from the analysis of the Z_{real} and the angular frequency (ω) components of the Warburg element. This evaluation is based on Fick's laws for semi-infinite linear diffusion model^[33] according to:

$$Z_{re} = R_{CT} + R_s + \sigma \omega^{-\frac{1}{2}} \quad (Eq. 1)$$

$$D_{Li} = \frac{R^2 T^2}{2 A^2 n^4 F^4 c^2 \sigma^2} \quad (Eq. 2)$$

$$Z_W = \sigma \omega^{-\frac{1}{2}} + \sigma(j\omega)^{-\frac{1}{2}} \quad (Eq. 3)$$

being: R , the ideal gas constant, $8.314 J (mol K)^{-1}$; T , the ambient temperature, 298 K; A , the electrode area, $\approx 0.5 cm^2$; n , the number of electrons transferred per molecule during the reaction ($1e^-$ per Li^+/Li process); F , the Faraday constant, $96485.3 C mol^{-1}$; c , the concentration of Li^+ in the electrolyte (1 M); and σ , the Warburg coefficient.

From the linear slope of the graphical representation of Z_{real} vs. $\omega^{-1/2}$ in the low frequency region, D_{Li+} value is obtained (Figure 8). According to these results, starting D_{Li+} of the **S@H₂P-COF-BATA** electrode is larger than the one corresponding to **S@H₂P-COF**. Comparing D_{Li+} values after continuous cycling, they decrease in both cases. More significantly, D_{Li+} in C rate mode is lower for **S@H₂P-COF** than for **S@H₂P-COF-BATA**, which maintains the same order of magnitude than the initial one. This evolution for D_{Li+} values in both compounds is in agreement with the values previously highlighted regarding the changes in specific capacity after continuous cycling and C rates mode, respectively.

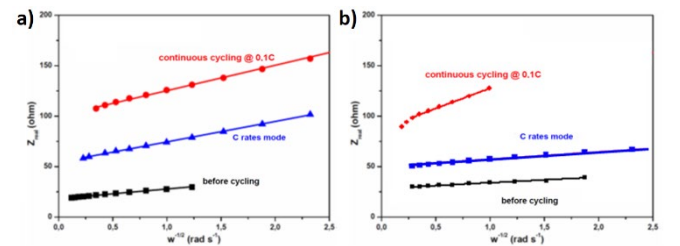


Figure 8. Z_{real} as a function of $w^{-1/2}$ for **S@H₂P-COF** (a) and **S@H₂P-COF-BATA** (b). Black: before cycling; blue: C rates mode; red: continuous cycling at 0.1C.

As expected, we have observed a general trend to decrease battery performance during the tests, being especially remarkable in the case of C rates mode for **S@H₂P-COF** electrode. Therefore, the **S@H₂P-COF-BATA** electrode provides better performance under demanding and/or changeable charge conditions than the **S@H₂P-COF** one.

S@H₂P-COF-based cathodes show inferior diffusion properties upon cycling, independently of the chosen test mode. The general worsening of the kinetic and diffusion parameters leads to an increase of the cell polarization, with the consequent performance loss. However, the presence of the covalent C-S bonds improves the sulphur use and provides faster ion diffusion pathways, mitigating the dissolution of polysulfide species into the electrolyte.

Conclusions

A novel porous, crystalline, porphyrin-based COF endowed with reactive allyl moieties (**H₂P-COF-BATA**) has been synthesized. **H₂P-COF-BATA** was subsequently inverse-vulcanized with sulfur, which provides an efficient method not only to physically confine polysulfides in the microporous channels but also to covalently bind them to the COF skeleton. For comparison purposes, polysulfides have been physically confined but without covalent linkage into an analogous COF yielding **S@H₂P-COF**. Both materials have been used as cathodes for rechargeable lithium-sulfur batteries.

S@H₂P-COF and **S@H₂P-COF-BATA** electrodes offer a general view of ageing upon cycling what is interpreted in terms of capacity loss and D_{Li^+} decreasing as result of the kinetic and diffusion parameters deterioration. On the other hand, chemical modification of **S@H₂P-COF** leading to **S@H₂P-COF-BATA**-based electrodes provides an obvious electrochemical performance improvement, especially significant under variable charge/discharge conditions. Such modification provides a new prospect material as electrode for sulphur batteries.

Considering the current amount of covalently bonded S in the COF cavity, battery performance is expected to significantly increase using a more efficient sulphur incorporation method to the COF.

Experimental Section

Materials and methods

The following reagents were commercially available and were used as received: *o*-DCB, *n*-butanol, sulfur, carbon Super P, polytetrafluoroethylene (PTFE), lithium bis(trifluoromethanesulfonyl)imide (LiTFSI), 1,3-dioxolane and 1,2-dimethoxyethane. 2,5-dihydroxyterephthalaldehyde (**DHTA**)^[34] and 5,10,15,20-tetrakis(4-aminophenyl)-21*H*,23*H*-porphyrin (**TAPP**)^[35] were synthesized according to the literature. The new 2,5-bis(allyloxy)terephthalaldehyde (**BATA**) was prepared according to the procedure described in the Supporting Information.

¹H NMR and ¹³C NMR spectra were recorded on a 300 MHz spectrometer. Chemical shifts are reported in ppm and referenced to the residual non-deuterated solvent frequencies (CDCl₃: δ 7.26 ppm for ¹H, 77.0 ppm for ¹³C). ¹³C Cross Polarization Magic Angle Spinning (CP-MAS) NMR spectra were recorded on a 400 MHz spectrometer Wide Bore (probe: 4 mm MAS WB DVT). The sample rotation frequency was 12 kHz and a 2.5 mm ZrO₂ rotor was used. Infrared spectra were registered on a Bruker Alpha-T ATR-FTIR spectrometer on a diamond plate. Powder X-ray diffraction measurements were carried out with X'PERT MPD with conventional Bragg-Brentano geometry using monochromatic Cu K_{α1} radiation (λ = 1.5406 Å) in the 2θ = 2°–40° range. Argon adsorption-desorption isotherms were measured at 87 K on an AutoSorb equipment (Quantachrome Instruments). Samples were previously degassed under high vacuum (<10⁻⁷ bar) for 4 h at 120 °C for **H₂P-COF** and **H₂P-COF-BATA** and at 60 °C for **S@H₂P-COF** and **S@H₂P-COF-BATA**. Thermogravimetric analysis was performed on a TGA-Q-50 instrument on a platinum plate, heating the samples under nitrogen atmosphere at a heating rate of 10 °C min⁻¹. Scanning electron microscopy (SEM) and energy-dispersive X-ray spectroscopy (EDX) were carried out using a JEOL JSM 6335F scanning electron microscope. The sample was dispersed over a slice of graphite adhesive and coated with gold by sputtering.

X-Ray Photoelectron Spectroscopy (XPS) experiments were performed in two different ultrahigh vacuum (UHV) chambers. In the first one, Mg K_α radiation excites core level photoelectrons, which are detected using a Specs Phoibos-150 electron analyzer with a constant pass energy of 20 eV. The second UHV chamber is located at the BACH beamline, receiving synchrotron light from the Elettra storage ring in Trieste (Italy). S_{2p} core level spectra were obtained using a photon energy of 850 eV and a Scienta R3000 electron analyzer. In this chamber, the polarization plane of the light was horizontal and coincided with the measuring plane. In both setups, the electron analyzer axis was fixed and coincided with the surface normal. The core level binding energies were calibrated using as references the binding energies of C 1s and Au 4f in contact with the sample. The line shape of core levels was fitted using a Shirley background and asymmetric singlet pseudo-Voigt functions. The fit was optimized using a Levenberg-Marquardt algorithm with a routine running in IGOR Pro (WaveMatrix Inc.).^[36] The quality of the fit was judged from a reliability factor, the normalized χ².

Synthesis

H₂P-COF was prepared according to a literature procedure with slight modifications.^[27] **TAPP** (200 mg, 0.30 mmol) and **DHTA** (99 mg, 0.60 mmol) were loaded into a Pyrex tube alongside 15 mL of an *o*-DCB/*n*-BuOH/3 M AcOH (1:2:0.3) mixture. The tube was degassed *via* three freeze-pump-thaw cycles, flame sealed and heated at 120 °C for 6 days. The resulting precipitate was filtered off, washed exhaustively with methanol, acetone and THF and dried under vacuum at 120 °C overnight, yielding a purple precipitate (258 mg, 93 %).

Similarly, **H₂P-COF-BATA** was synthesized by loading **TAPP** (203 mg, 0.30 mmol), **DHTA** (75 mg, 0.45 mmol) and **BATA** (37 mg, 0.15 mmol) into a Pyrex tube to which were added 15 mL of an *o*-DCB/*n*-BuOH/3 M AcOH (1:2:0.3) mixture. The tube was degassed *via* three freeze-pump-thaw cycles, flame sealed and heated at 120 °C for 6 days. The resulting precipitate was filtered off, washed exhaustively with methanol, acetone and THF, and dried under vacuum at 120 °C overnight, yielding a purple precipitate (275 mg, 94 %).

S@H₂P-COF-BATA and **S@H₂P-COF** were prepared by the melt-diffusion strategy. **H₂P-COF-BATA** or **H₂P-COF** were mixed with elemental sulfur in a 1:1 weight ratio and grinded uniformly in an agate mortar. The mixtures were transferred into a round bottom flask and heated at 120 °C overnight under an argon atmosphere, so sulfur can diffuse into the COFs pores, and then at 185 °C for an additional 8 hours causing sulfur to undergo radical polymerization with the accessible allyl

groups in the pores of **H₂P-COF-BATA**. Finally, the materials were heated at 185 °C under argon flow to remove surface sulfur.

Electrochemistry

All electrochemical experiments were carried out using 2032 coin-cell type batteries with lithium foil as both anode and reference electrode. The sulfur cathode was prepared by mortar mixing the corresponding active material with carbon Super P (TIMCAL) and PTFE (Aldrich) as binder in a 60:30:10 weight proportion. The active material (host material) has low conductivity and a large amount of the conductive carbon (30 %) was used. After drying at 80 °C for 12 h, the electrode material is pelletized into 8 mm diameter pellets (and ≈ 8 mg active material). Cells were assembled in an Ar filled glove box using microporous 25 µm thickness Celgard membrane (2325 Celgard) as separator. Approximately 1 mL of 1 M LiTFSI (99.95 %) in 1,3-dioxolane (DOL) and 1,2-dimethoxyethane (DME) (DOL:DME in 1:1 volume ratio, Aldrich, 99.9 %) electrolyte was added to the cells. The galvanostatic discharge/charge tests were performed in the voltage range of 1.80–2.70 V at different C/n rates (being “n” the number of hours to reduce/oxidize 1 Li) using an Arbin Instruments BT2143 workstation. Experiments were done at room temperature, without isothermal setup conditions. Similarly, Electrochemical Impedance Spectroscopy (EIS) and Cyclic Voltammetry (CV) were conducted using Autolab electrochemical system II PGSTAT30 (Ecochemie) impedance analyzer. EIS measurements were carried out at open circuit potential in the frequency range between 100 kHz and 1 mHz with an applied voltage of 0.01 V using a two-probe method. ZView 3.1 software (Scribner Ass.) was employed to assess the results. CV measurements were carried out in the 1.80–2.70 V voltage range at different scan rates, from 0.1 to 1 mV s⁻¹.

Acknowledgements

Financial support from Spanish Government (Projects MAT2016-77608-C3-1-P, MAT2016-77608-C3-2-P, FIS2017-82415-R, ENE2016-77055-C3-1-R), the “María de Maeztu” Programme for Units of Excellence in R&D (MDM-2014-0377) and the UCM (INV.GR.00.1819.10759) is acknowledged. We thank the BACH beamline team at Elettra for technical assistance with XPS measurements. The research leading to these results has received funding from the European Community's Horizon 2020 Framework Programme under grant agreement No 730872.

Keywords: Li-S batteries • shuttle effect • electrochemical impedance spectroscopy • inverse vulcanization • covalent organic frameworks

- [1] J. B. Goodenough, K.-S. Park, *J. Am. Chem. Soc.* **2013**, *135*, 1167–1176.
- [2] a) D. Peramunage, S. Licht, *Science* **1993**, *261*, 1029; b) A. Manthiram, Y. Fu, S.-H. Chung, C. Zu, Y.-S. Su, *Chem. Rev.* **2014**, *114*, 11751–11787.
- [3] Z. Lin, Z. Liu, W. Fu, N. J. Dudney, C. Liang, *Angew. Chem. Int. Ed.* **2013**, *52*, 7460–7463.
- [4] a) Y. V. Mikhaylik, J. R. Akridge, *J. Electrochem. Soc.* **2004**, *151*, A1969–A1976; b) B. L. Ellis, K. T. Lee, L. F. Nazar, *Chem. Mater.* **2010**, *22*, 691–714; c) C. Barchasz, J.-C. Leprêtre, F. Alloin, S. Patoux, *J. Power Sources* **2012**, *199*, 322–330; d) M.-K. Song, E. J. Cairns, Y. Zhang, *Nanoscale* **2013**, *5*, 2186–2204.
- [5] X. Ji, K. T. Lee, L. F. Nazar, *Nat. Mater.* **2009**, *8*, 500.
- [6] a) J. Sun, A. Klechikov, C. Moise, M. Prodana, M. Enachescu, A. V. Talyzin, *Angew. Chem. Int. Ed.* **2018**, *57*, 1034–1038; b) Y. Zhang, J. Wang, S. N. Riduan, *J. Mater. Chem. A* **2016**, *4*, 14902–14914; c) D. Chen, A.-J. Avestro, Z. Chen, J. Sun, S. Wang, M. Xiao, Z. Erno, M. M. Algaradah, M. S. Nassar, K. Amine, Y. Meng, J. F. Stoddart, *Adv. Mater.* **2015**, *27*, 2907–2912.
- [7] a) G. Zheng, Q. Zhang, J. J. Cha, Y. Yang, W. Li, Z. W. Seh, Y. Cui, *Nano Lett.* **2013**, *13*, 1265–1270; b) W. Zhou, X. Xiao, M. Cai, L. Yang, *Nano Lett.* **2014**, *14*, 5250–5256; c) S. Zheng, F. Yi, Z. Li, Y. Zhu, Y. Xu, C. Luo, J. Yang, C. Wang, *Adv. Funct. Mater.* **2014**, *24*, 4156–4163; d) Z. Cheng, H. Pan, H. Zhong, Z. Xiao, X. Li, R. Wang, *Adv. Funct. Mater.* **2018**, *28*, 1707597.
- [8] a) J.-S. Kim, T. H. Hwang, B. G. Kim, J. Min, J. W. Choi, *Adv. Funct. Mater.* **2014**, *24*, 5359–5367; b) A. G. Simmonds, J. J. Griebel, J. Park, K. R. Kim, W. J. Chung, V. P. Oleshko, J. Kim, E. T. Kim, R. S. Glass, C. L. Soles, Y.-E. Sung, K. Char, J. Pyun, *ACS Macro Lett.* **2014**, *3*, 229–232; c) W. J. Chung, J. J. Griebel, E. T. Kim, H. Yoon, A. G. Simmonds, H. J. Ji, P. T. Dirlam, R. S. Glass, J. Wie, N. A. Nguyen, B. W. Guralnick, J. Park, Á. Somogyi, P. Theato, M. E. Mackay, Y.-E. Sung, K. Char, J. Pyun, *Nat. Chem.* **2013**, *5*, 518–524.
- [9] H. Kim, J. Lee, H. Ahn, O. Kim, M. J. Park, *Nat. Commun.* **2015**, *6*, 7278.
- [10] S. N. Talapaneni, T. H. Hwang, S. H. Je, O. Buyukcakil, J. W. Choi, A. Coskun, *Angew. Chem. Int. Ed.* **2016**, *55*, 3106–3111.
- [11] a) X. Feng, X. Ding, D. Jiang, *Chem. Soc. Rev.* **2012**, *41*, 6010–6022; b) S.-Y. Ding, W. Wang, *Chem. Soc. Rev.* **2013**, *42*, 548–568; c) J. W. Colson, W. R. Dichtel, *Nat. Chem.* **2013**, *5*, 453–465; d) A. P. Côté, A. I. Benin, N. W. Ockwig, M. Keffe, A. J. Matzger, O. M. Yaghi, *Science* **2005**, *310*, 1166.
- [12] a) G. Maurin, C. Serre, A. Cooper, G. Férey, *Chem. Soc. Rev.* **2017**, *46*, 3104–3107; b) C. S. Diercks, O. M. Yaghi, *Science* **2017**, *355*, eaal1585; c) N. Huang, P. Wang, D. Jiang, *Nat. Rev. Mater.* **2016**, *1*, 16068; d) M. S. Lohse, T. Bein, *Adv. Funct. Mater.* **2018**, *28*, 1705553.
- [13] a) J. Zhou, B. Wang, *Chem. Soc. Rev.* **2017**, *46*, 6927–6945; b) P. Xiao, Y. Xu, *J. Mater. Chem. A* **2018**, *6*, 21676–21695; c) S. B. Alahakoon, C. M. Thompson, G. Occhialini, R. A. Smaldone, *ChemSusChem* **2017**, *10*, 2116–2129.
- [14] F. Xu, S. Jin, H. Zhong, D. Wu, X. Yang, X. Chen, H. Wei, R. Fu, D. Jiang, *Sci. Rep.* **2015**, *5*, 8225.
- [15] a) H. Liao, H. Ding, B. Li, X. Ai, C. Wang, *J. Mater. Chem. A* **2014**, *2*, 8854–8858; b) F. Xu, S. Yang, G. Jiang, Q. Ye, B. Wei, H. Wang, *ACS Appl. Mater. Interfaces* **2017**, *9*, 37731–37738; c) S. H. Je, H. J. Kim, J. Kim, J. W. Choi, A. Coskun, *Adv. Funct. Mater.* **2017**, *27*, 1703947.
- [16] a) H. Liao, H. Wang, H. Ding, X. Meng, H. Xu, B. Wang, X. Ai, C. Wang, *J. Mater. Chem. A* **2016**, *4*, 7416–7421; b) Y. Meng, G. Lin, H. Ding, H. Liao, C. Wang, *J. Mater. Chem. A* **2018**, *6*, 17186–17191.
- [17] a) Q. Jiang, Y. Li, X. Zhao, P. Xiong, X. Yu, Y. Xu, L. Chen, *J. Mater. Chem. A* **2018**, *6*, 17977–17981; b) Y. Wu, Z. Zhang, S. Bandow, K. Awaga, *Bull. Chem. Soc. Jpn.* **2017**, *90*, 1382–1387; c) D.-G. Wang, N. Li, Y. Hu, S. Wan, M. Song, G. Yu, Y. Jin, W. Wei, K. Han, G.-C. Kuang, W. Zhang, *ACS Appl. Mater. Interfaces* **2018**, *10*, 42233–42240.
- [18] J. L. Segura, S. Royuela, M. Mar Ramos, *Chem. Soc. Rev.* **2019**, *Advance Article*, doi: 10.1039/C9CS00978C.
- [19] a) X. Feng, L. Liu, Y. Honsho, A. Saeki, S. Seki, S. Irle, Y. Dong, A. Nagai, D. Jiang, *Angew. Chem. Int. Ed.* **2012**, *51*, 2618–2622; b) S. Wan, F. Gándara, A. Asano, H. Furukawa, A. Saeki, S. K. Dey, L. Liao, M. W. Ambrogio, Y. Y. Botros, X. Duan, S. Seki, J. F. Stoddart, O. M. Yaghi, *Chem. Mater.* **2011**, *23*, 4094–4097; c) M. Calik, F. Auras, L. M. Salonen, K. Bader, I. Grill, M. Handloser, D. D. Medina, M. Dogru, F. Löbermann, D. Trauner, A. Hartschuh, T. Bein, *J. Am. Chem. Soc.* **2014**, *136*, 17802–17807.
- [20] S. Kandambeth, D. B. Shinde, M. K. Panda, B. Lukose, T. Heine, R. Banerjee, *Angew. Chem. Int. Ed.* **2013**, *52*, 13052–13056.
- [21] X.-g. Yu, J.-y. Xie, J. Yang, H.-j. Huang, K. Wang, Z.-s. Wen, *J. Electroanal. Chem.* **2004**, *573*, 121–128.
- [22] J. P. Macquet, M. M. Millard, T. Theophanides, *J. Am. Chem. Soc.* **1978**, *100*, 4741–4746.
- [23] a) A. G. Schaufuß, H. W. Nesbitt, I. Kartio, K. Laajalehto, G. M. Bancroft, R. Szargan, *J. Electron Spectrosc. Relat. Phenom.* **1998**, *96*, 69–82; b) W. Li, M. Zhou, H. Li, K. Wang, S. Cheng, K. Jiang, *Energy Environ. Sci.* **2015**, *8*, 2916–2921.
- [24] a) D. Sun, J. Yang, X. Yan, *Chem. Commun.* **2015**, *51*, 2134–2137; b) S. Yang, L. Zhi, K. Tang, X. Feng, J. Maier, K. Müllen, *Adv. Funct. Mater.* **2012**, *22*, 3634–3640; c) L. Xiao, Y. Cao, J. Xiao, B. Schwenzer, M. H. Engelhard, L. V. Saraf, Z. Nie, G. J. Exarhos, J. Liu, *Adv. Mater.* **2012**, *24*, 1176–1181.
- [25] H. Xu, X. Chen, J. Gao, J. Lin, M. Addicoat, S. Irle, D. Jiang, *Chem. Commun.* **2014**, *50*, 1292–1294.
- [26] C. S. Diercks, S. Lin, N. Kornienko, E. A. Kapustin, E. M. Nichols, C. Zhu, Y. Zhao, C. J. Chang, O. M. Yaghi, *J. Am. Chem. Soc.* **2018**, *140*, 1116–1122.
- [27] N. Huang, R. Krishna, D. Jiang, *J. Am. Chem. Soc.* **2015**, *137*, 7079–7082.

- [28] L. Chen, K. Furukawa, J. Gao, A. Nagai, T. Nakamura, Y. Dong, D. Jiang, *J. Am. Chem. Soc.* **2014**, *136*, 9806-9809.
- [29] Z. A. Ghazi, L. Zhu, H. Wang, A. Naeem, A. M. Khattak, B. Liang, N. A. Khan, Z. Wei, L. Li, Z. Tang, *Adv. Energy Mater.* **2016**, *6*, 1601250.
- [30] H. Qu, J. Zhang, A. Du, B. Chen, J. Chai, N. Xue, L. Wang, L. Qiao, C. Wang, X. Zang, J. Yang, X. Wang, G. Cui, *Adv. Sci.* **2018**, *5*, 1700503.
- [31] M. Marinescu, L. O'Neill, T. Zhang, S. Walus, T. E. Wilson, G. J. Offer, *J. Electrochem. Soc.* **2018**, *165*, A6107–A6118.
- [32] B. A. Boukamp, *Solid State Ion.* **1986**, *20*, 31–44.
- [33] A. Lasia, *Electrochemical Impedance Spectroscopy and its Applications*, Springer-Verlag, New York, **2014**.
- [34] Y. Okada, M. Sugai, K. Chiba, *J. Org. Chem.* **2016**, *81*, 10922–10929.
- [35] M. Yuasa, K. Oyaizu, A. Yamaguchi, M. Kuwakado, *J. Am. Chem. Soc.* **2004**, *126*, 11128–11129.
- [36] M. Schmid, H.-P. Steinrück, J. M. Gottfried, *Surf. Interface Anal.* **2014**, *46*, 505–511.